

# Time-sequenced flow field prediction in an optical spark-ignition direct-injection engine using bidirectional recurrent neural network (bi-RNN) with long short-term memory

Fengnian Zhao<sup>a,c</sup>, Zhiming Ruan<sup>a</sup>, Zongyu Yue<sup>b,c,\*</sup>, David L.S. Hung<sup>a,d,\*</sup>, Sibendu Som<sup>c</sup>, Min Xu<sup>d</sup>

<sup>a</sup> University of Michigan-Shanghai Jiao Tong University Joint Institute, Shanghai Jiao Tong University, 200240 Shanghai, China

<sup>b</sup> State Key Laboratory of Engines, Tianjin University, 300072 Tianjin, China

<sup>c</sup> Argonne National Laboratory, 60439 Lemont, IL, USA

<sup>d</sup> Institute of Automotive Engineering, School of Mechanical Engineering, Shanghai Jiao Tong University, 200240 Shanghai, China



## HIGHLIGHTS

- Bi-RNN model is used for predicting time-sequenced flow fields in a SIDI engine.
- Flow structure & magnitude validation are used as model performance criteria.
- Prediction results of machine learning model matched well with experimental data.
- The proposed method can improve the temporal resolution in flow measurements.

## ARTICLE INFO

### Keywords:

Optical SIDI engine  
In-cylinder flow prediction  
Bi-RNN model  
Local & global comparison methods

## ABSTRACT

To further improve the energy conversion efficiency of internal combustion engine, the transient and complex air flow movement inside the cylinder needs to be better understood and controlled. Although the in-cylinder flow fields are highly stochastic with strong cycle-to-cycle fluctuations, machine learning can still provide an efficient way to learn and regress the complex flow movement process inside the cylinder. In this work, a bidirectional recurrent neural network (bi-RNN) model with long short-term memory was applied to predict the in-cylinder flow fields at different time steps using training data from multi-cycle particle image velocimetry (PIV) measurements. To evaluate the agreement between the true and predicted flow fields, structure and magnitude comparison indices are calculated both globally and locally. The comparison results show that the bi-RNN model can accurately predict the bulk flow and vortex motions from early intake stroke to compression stroke. This work demonstrates that the machine learning model has the potential to predict the underlying dynamics of the interaction between in-cylinder flows and provides a reliable way to improve temporal resolution in PIV flow data to better reveal transient in-cylinder flow features.

## 1. Introduction

To fulfill the strict requirements for internal combustion engines in terms of emissions and fuel consumption, the spark-ignition direct-injection (SIDI) engine has become a mainstream technology for the automotive industry. In this engine, the in-cylinder flow characteristic and its cycle-to-cycle variations affect the working processes of fuel vaporization, fuel-air mixing, and combustion stability [1–4]. Rising temperature and pressure in the cylinder during compression stroke impact the dispersion of fuel vapor as intake air tumbles and swirls intermittently during every individual engine cycle. A literature survey

of cyclic variability in SI engine by Ozdor et al. [5] shows that the combustion variations are associated with loss of output power and thermal efficiency, and eliminating of the cyclic variations could improve the engine output power by 10% for the same fuel consumption. Due to higher fluctuating energy, the spatial and temporal variations of coherent large scale flow structures usually play a dominant role triggering the cyclic variability of the combustion, such as the partial stratification of fuel-air mixture and random heat transfer from the burning kernel to the spark plug [5–8]. Many researchers have utilized the flow decomposition methods to extract and analyze the flow coherent structures from the velocity fields of different engine cycles

\* Corresponding authors.

E-mail addresses: [zongyuyue@tju.edu.cn](mailto:zongyuyue@tju.edu.cn) (Z. Yue), [dhung@sjtu.edu.cn](mailto:dhung@sjtu.edu.cn) (D.L.S. Hung).

[9–11]. To reduce the cycle-to-cycle variations and improve thermal efficiency, SI engines as well as other heat systems usually introduce strong tumble or swirl vortex during the intake stroke [11–15]. These stable and transient flow structures could enhance the fuel spray mixing and increase the turbulence intensity due to the breakdown of large-scale flow structure at the end of the compression stroke [1]. In addition, the homogeneous fuel-air mixture and enhanced turbulence intensity could increase the burning speed, which reduces the time for heating the end gas ahead of the flame and lowering the engine knocking likelihood. With these proven benefits of flow structures to enhance the thermal process in engine cylinder, it is necessary to acquire a panoramic understanding of in-cylinder flow field characteristics.

As one of the most commonly used optical diagnostics techniques in engine research, particle image velocimetry (PIV) can make highly resolved spatial and temporal in-cylinder flow measurements to reveal the coherent flow structure [16–21]. With crank-angle-resolved in-cylinder flow measurements over massive numbers of engine cycles, researchers can study the ensemble flow of multiple cycles as well as the cycle-to-cycle variation characteristics. However, transient 3D characteristics of in-cylinder flow and its cyclic variations still remain a big concern in engine flow investigations.

A few researchers have applied advanced 3D PIV techniques to describe the 3D features of in-cylinder flow. Baum et al. [19] used tomographic PIV to visualize 3D in-cylinder flow structures, but only within a small (millimetric) volume of thickness. To enlarge the volume of measurements, other researchers preferred to use multi-plane PIV to reveal the 3D flow characteristics. Zhao et al. [20] applied planar PIV on five planes to investigate 3D flow features of ensemble-averaged flow fields. However, ensemble flow analysis has its limitations with respect to cycle-to-cycle variation issues, and measurements that enable a complete capture of multi-plane instantaneous flow features are still needed. Buhl et al. [21] and Bode et al. [16] utilized an innovative PIV setup to achieve a quasi-simultaneous multi-plane PIV measurement, which can record flow fields in different planes within a short time difference. However, correlating flow features of different planes can be problematic because of the lag between PIV measurements if the flow is highly transient, such as under high-engine-speed conditions. Another experimental limitation is that the temporal and spatial resolutions cannot both be maximized while recording data from massive numbers of engine cycles because of the limitations in random-access memory and readout rates of the high-speed camera. A trade-off is usually made between temporal resolution, spatial resolution and recorded engine cycles. However, lower temporal or spatial resolutions would affect capture of transient flow features, and flow data from fewer engine cycles could be insufficient for analysis of cycle-to-cycle variations. Additionally, the size of the image from tomographic PIV and multi-plane PIV measurements could be much larger than that from planar PIV measurement. Therefore, it is still a daunting task for researchers to develop techniques to capture transient 3D or multi-plane flow-field data for large numbers of engine cycles.

To eliminate the time-lag effects and increase the temporal resolution without sacrificing the spatial resolution and recorded engine cycles, prediction of time-sequenced flow development using machine learning models could be a solution, since the machine learning approach has a superior ability to learn and regress the non-linear process. Flow development, fuel-air mixing, and combustion are all non-linear processes with highly transient features, which are suitable for machine learning applications. Many engine researchers have begun to apply machine learning methods to data analysis and prediction. For instance, Kodavasal et al. [22] applied the random forest algorithm to analyze cyclic variations of multiple engine cycles obtained from large-eddy simulation. The random forest model shows a good ability to learn the relationship between the flow-field features before ignition and the peak cylinder pressure. Recently, Hanuschkin et al. [23] also concentrated on machine learning applications for using flow-field features

to predict engine performance. The flow data from mid-cylinder and mid-valve planes were recorded by PIV measurements. The trained multilayer perceptron and boosted decision tree models both indicated that the basic in-cylinder flow features at –180 CAD after top dead center (ATDC) at the mid-cylinder plane were sufficient to predict whether the combustion cycles were of high or low indicated mean effective pressure. Moiz et al. [24] utilized a machine learning-genetic algorithm (ML-GA) with a computational fluid dynamics (CFD) engine model to learn the non-linear relationship between input parameters, like fuel injection strategy and injector design, and target outputs like engine performance and emissions. Using ML-GA decreased the computational cost by at least 75%, by reducing the number of CFD runs for optimization problems, without accuracy loss. Other machine learning algorithms like the K-means clustering algorithm and artificial neural networks (ANNs) are also widely used for analyzing engine data, such as soot formation and particulate matter distributions [25,26]. Among these machine learning algorithms, the ANN model plays an important role in engine prediction problems, since it is considered more accurate in dealing with complicated problems if enough layers are used and adequate data are available. However, the training process for the ANN model usually takes a relatively long computational time compared with other algorithms. Many engine researchers use a feedforward ANN model for engine prediction problems. Engine performance and emission predictions based on the ANN model for gasoline, diesel or dual-fuel engines have been proven to have a high accuracy [27–34].

Unlike feedforward ANNs, the recurrent neural network (RNN) is a machine learning model that is capable of processing sequential inputs, allowing it to exhibit dynamic temporal behavior for a time sequence. A special type of RNN, the long short-term memory (LSTM)-based RNN model, could perform classification or prediction on the basis of the hidden and cell states stored in the LSTM cells [35]. The LSTM cells perform better in mitigating the exploding and vanishing problems in the training process, compared with traditional RNN; therefore, the LSTM-based RNN model is widely used for natural language processing (NLP), speech recognition, and time series prediction [36,37]. In short, an RNN model can remember information that it encountered previously and make predictions based on the memory. A bidirectional RNN (bi-RNN) model is comprised of two RNN models that process inputs in opposite directions. It provides predictions at the current time-step, based on the stored information acquired before and after the current time-step, with higher accuracy compared to the RNN model.

As expected, different types of neural networks are designed for different datasets. RNN is a specialized ANN for modeling and regressing time sequential data. It performs well in prediction problems based on the memory of previous dataset, whereas the bi-RNN is more suitable in this study since the prediction is based on the flow data in both previous and future time steps. Among the variants of bi-RNNs, the LSTM based network becomes more popular because it can overcome the vanishing gradient problem [35] often found in traditional bi-RNNs. Thus, in the present work, a bi-RNN model comprised of two LSTM-based RNN models is utilized for predicting the time-sequenced flow fields. The PIV experiments are conducted under high intake air swirl ratio. The datasets in this study are the flow fields recorded from –300 CAD ATDC to –98 CAD ATDC over 100 cycles. The recording resolution of PIV measurements is 2 CAD, resulting in a total of 10,000 velocity fields for a single test condition. The inputs to the bi-RNN model are two flow fields with a crank angle difference of 4 CAD, and the flow field at the median crank angle is the output. The bi-RNN model is used to learn the underlying dynamics of the flow interactions. With a well-trained bi-RNN model, PIV measurements can be obtained at a higher temporal resolution (the resolution improved from 4 CAD to 2 CAD in this study).

## 2. Experimental setup

The PIV experiment was carried out in a 0.55-L single-cylinder

**Table 1**  
Engine Operating and PIV Measurement Parameters.

Parameter	Value
<i>Engine and Operation Parameters</i>	
Engine speed	800 rpm
Bore	86 mm
Stroke	94.6 mm
Clearance volume	49.96 cm <sup>3</sup>
Displacement	549.51 cm <sup>3</sup>
Compression ratio	12:1
Manifold absolute pressure	100 kPa (absolute)
Swirl & tumble ratios	5.68 & 0.55
<i>PIV Measurement Parameters</i>	
Seeding particle	Silicone oil
Mean Particle diameter	1 $\mu$ m
Laser energy	4.2 mJ/pulse
Time interval between 2 laser pulses	20 $\mu$ s
Interrogation size and overlap	32 $\times$ 32 pixels and 50%
Field of view	77.8 mm $\times$ 77.8 mm
Spatial resolution	0.15 mm/pixel

optical SIDI engine with four valves. The experimental data used in the present study were obtained previously by Zhao et al. [18]. Table 1 lists the key parameters of engine operation and PIV measurement. A schematic of the PIV experimental setup and a view of the swirl plane and the velocity field after processing are shown in Fig. 1. The PIV system consists mainly of a double-pulsed Nd:YLF laser with a 527-nm wavelength (Litron LDY303HE) and a high-speed camera (Phantom V7.3), which operated at 2400 Hz to record a pair of images (2 CADs/image). The location of the focal plane in this study is 30 mm below the injector tip. The field of view of the image is 77.8 mm  $\times$  77.8 mm, and the view of the measured swirl plane represents a 62-mm-diameter viewable area. The PIV processing software used is DaVis 8.3 (LaVision), and the spatial resolution of the processed flow data is 25  $\times$  25 vectors per flow field.

### 3. Methodology

#### 3.1. LSTM based bidirectional recurrent neural networks (bi-RNN)

A bi-RNN model is a machine learning model that has the ability to process sequential inputs, allowing it to exhibit dynamic temporal behavior. It is comprised of two RNN models that process inputs in

opposite directions, enabling full use of information before and after the target time step in the entire sequence. Fig. 2a and b show the schematic configurations, including input, output, and hidden layers, of an RNN model and a bi-RNN model, respectively [36]. X and Y represent the inputs and outputs of the models, and the subscript t stands for the time step. However, the traditional RNN and Bi-RNN models could encounter the exploding and vanishing problems in the training process. To solve these problems, LSTM cells were introduced by Hochreiter [35]. As shown in Fig. 2c, each LSTM cell has three multiplicative gates, i.e., the input, output, and forget gates. These gate configurations allow the LSTM cell to store and obtain information over longer periods of time so that LSTM-based neural networks are better at mitigating the problems of gradient vanishing. H and C represent the hidden state and cell state of the LSTM cells, respectively. The LSTM transition equations are shown as follows:

$$f_t = \sigma(W_f \otimes [h_{t-1}, X_t]) \quad (1)$$

$$i_t = \sigma(W_i \otimes [h_{t-1}, X_t]) \quad (2)$$

$$o_t = \sigma(W_o \otimes [h_{t-1}, X_t]) \quad (3)$$

$$C_t = f_t \otimes C_{t-1} + i_t \otimes C_t \quad (4)$$

$$C_t = \tanh(W_C \otimes [h_{t-1}, X_t]) \quad (5)$$

$$h_t = o_t \otimes \tanh(C_t) \quad (6)$$

where  $X_t$  is the cell input and  $h_t$  is the cell output.  $f_t$ ,  $i_t$  and  $o_t$  represent the forget, input and output gates, respectively. The entries of these gating vectors  $f_t$ ,  $i_t$  and  $o_t$  determine the open (=1) and close (=0) of these gates.  $C_t$  and  $C_{t-1}$  represent the cell state and updated cell state, respectively.  $W$  terms are weight metrics of different gates and  $\otimes$  is the element-wise multiply operator. In those equations, bias terms are ignored. In training process, the weight and bias metrics will be learned and updated.  $\sigma$  is the sigmoid function, and  $\tanh$  is the hyperbolic tangent function. Fig. 2c shows the calculation of the cell state is controlled by the forget gate and only with some linear interactions. Therefore, the cell state between each time-step will not vary a lot such that the LSTM cell can store and obtain information over longer periods of time.

In this work, the target is to predict the flow data in the middle time step using two flow fields at different CADs. A LSTM-based bi-RNN model is more suitable for this task, since the prediction is processed in

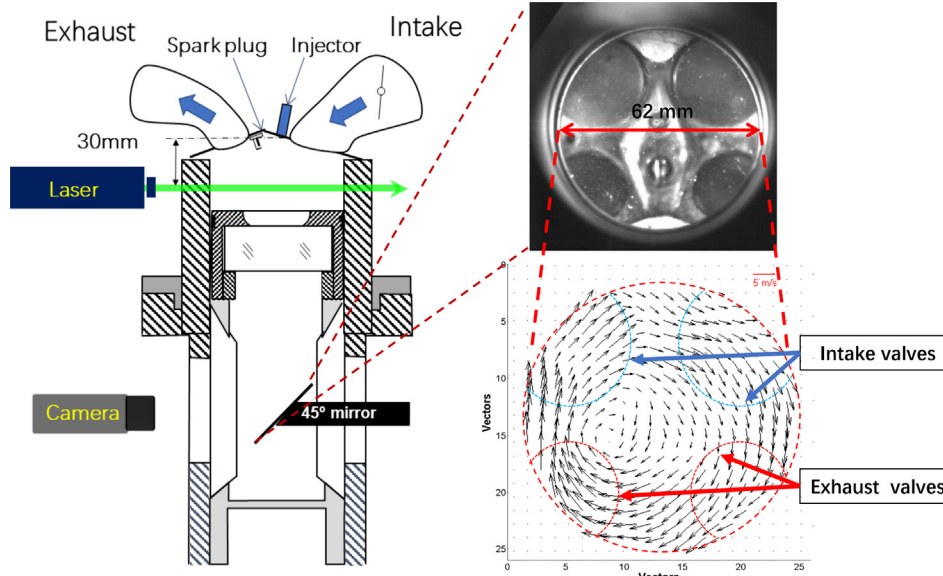


Fig. 1. Experimental schematic with view of swirl plane.

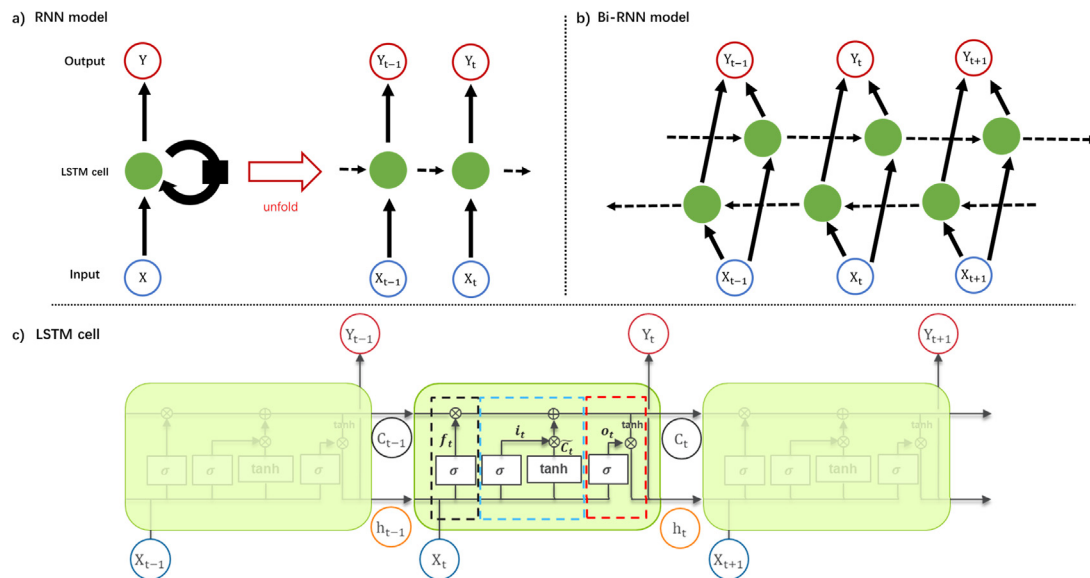


Fig. 2. Configurations of (a) an RNN model, (b) a bi-RNN model and (c) LSTM cells.

two directions.

In NLP or speech recognition, a paragraph or a sentence is generated word by word. The same idea is applied in the flow-field prediction, wherein the target flow field is predicted vector by vector. In this way, the output of our bi-RNN model is a single vector at a specific location. Considering that the target flow vector will be strongly influenced by its neighbor flows, the vectors surrounding the output vector are used as the inputs. The input format is shown in Eq. (7).

$$\text{Inputs} = \begin{matrix} \bar{v}_{(x-4,y-4)}, t_{p-j} & \cdots & \bar{v}_{(x-4,y+4)}, t_{p-j} \\ \vdots & & \vdots \\ \bar{v}_{(x+4,y-4)}, t_{p-j} & \cdots & \bar{v}_{(x+4,y+4)}, t_{p-j} \end{matrix} \quad (7)$$

where  $j = -1$  and  $1$  indicate the time steps prior to and following the predicted time step  $t_p$ . The input size is  $9 \times 9$ , and the coordinate  $(x, y)$  indicates the target vector position. With the inputs of two  $9 \times 9$  flow fields, the LSTM cells can calculate and update the weights and bias metrics. The activation functions sigmoid and tanh are used in LSTM cells (Fig. 2c). In short, two  $9 \times 9$  flow fields at the previous and later time steps are used to predict the flow field vector-by-vector at the target time step (Fig. 3). It is worth mentioning that the  $9 \times 9$  vector field located at the center of the original  $25 \times 25$  flow fields is the output of the bi-RNN model. The reason is that the vectors outside the central  $9 \times 9$  vector field do not have enough surrounding vectors as input.

Since vectors with small magnitudes, such as the vectors near the vortex motion, are usually hard to predict, the loss function should lower the impacts of the mismatch of small-magnitude vectors. Therefore, a quadratic loss function, which can also be considered as the mean square error (MSE), is chosen as the loss function in our bi-RNN model (Eq. (8)):

$$\text{MSE} = \frac{1}{2n} \sum_{i=1}^n ((\hat{v}_x^i - v_x^i)^2 + (\hat{v}_y^i - v_y^i)^2) \quad (8)$$

where  $\hat{v}$  is the velocity vector in the true flow fields,  $v$  is the predicted velocity vector, and  $n$  is the batch size. To reach the global minimum of the loss function, the Adam optimization algorithm [35] is used to update the weight matrices.

### 3.2. Predictor performance criteria - structure and magnitude comparison of vector fields

In this study, structure and magnitude comparison indices [20] are

used to quantitatively evaluate the similarity between true and predicted flow fields. The structure index (also known as relevance index) and magnitude index are defined as follows:

$$\text{Structure Index} = \frac{(\hat{v} \cdot v)}{\|\hat{v}\| \|v\|} \quad (9)$$

$$\text{Magnitude Index} = 1 - \left| \frac{\|\hat{v}\| - \|v\|}{\|\hat{v}\| + \|v\|} \right| \quad (10)$$

The structure index is used to evaluate the angle between two vectors. The range of the structure index is from  $-1$  to  $1$ . A value of  $1$  means the two vectors are perfectly aligned, and  $-1$  means the two vectors are in opposite directions. The magnitude index is used to evaluate the magnitude difference between two vectors. The range is from  $0$  to  $1$ . A larger value of magnitude index means higher similarity. A value of  $1$  means two vector magnitudes are identical.

To evaluate the similarity between flow fields, the averaged structure index and magnitude index of every vector inside the flow fields provides a single value to check the overall similarities of velocity directions and magnitudes. The averaged structure and global magnitude indices are referred to as global structure and global magnitude indices (GSI and GMI, respectively) in this work. GSI and GMI are capable of showing the trends of similarities of different CADs from the intake to the compression stroke. Meanwhile, the maps of local structure and local magnitude indices (LSI and LMI) can provide a local point-by-point comparison, which shows the detailed comparison with spatial information.

### 3.3. Model building process

#### 3.3.1. Overview of the method

In this study, the open-source code Tensorflow [38], based on Python, was implemented to build the bi-RNN model. Fig. 4 shows the workflow for building a bi-RNN model for flow-field prediction. In total, the data from  $-300$  CAD ATDC to  $-98$  CAD ATDC (102 different crank angles) for 100 consecutive cycles were captured by PIV measurements. First, the total flow data were randomly divided into training (80%) and test (20%) sets by engine cycles. For both the training and test datasets, only 100 different crank angles, i.e., from  $-298$  CAD to  $-100$  CAD, were selected as the crank angle range for prediction in this study. Second, the training process was conducted to train the bi-RNN learner. As shown in Fig. 4, in every single cycle, the flow fields at each of 3 sequential crank angles are grouped as a unit.

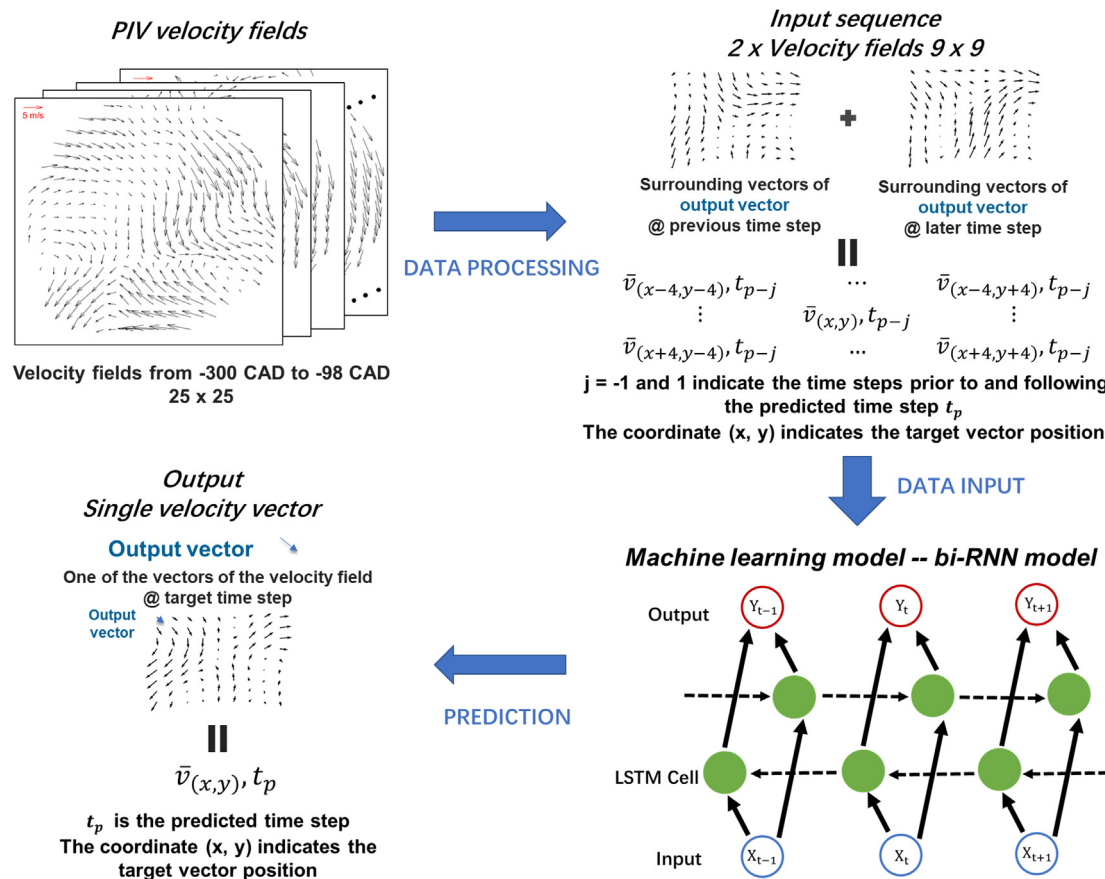


Fig. 3. Schematic diagram of prediction process.

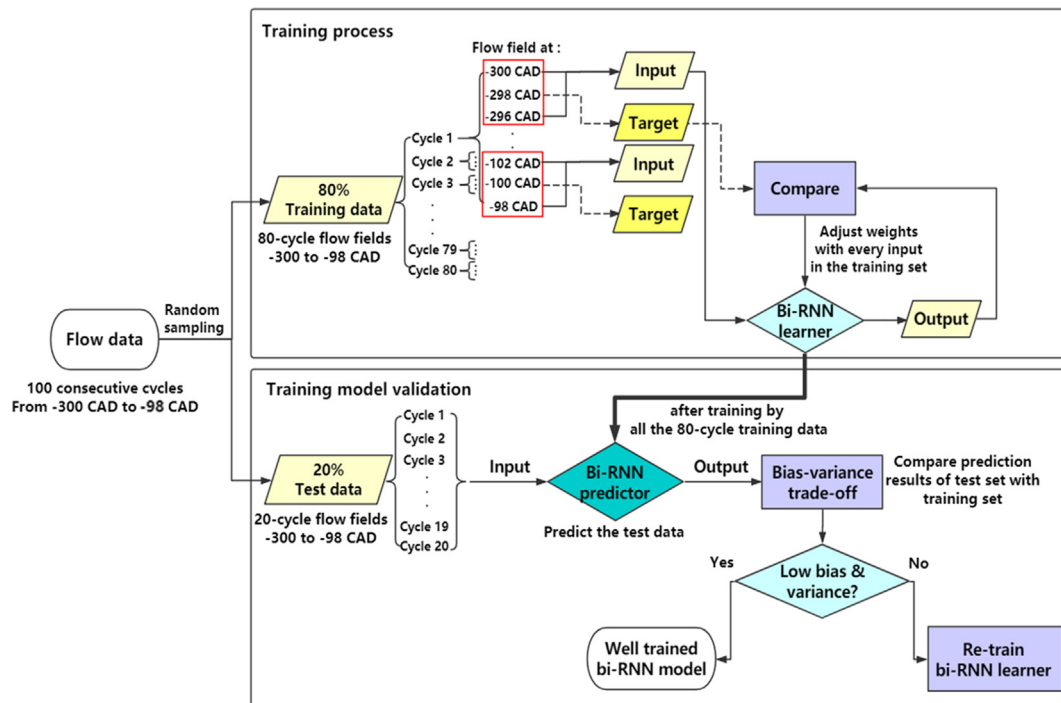


Fig. 4. Workflow for bi-RNN model building.

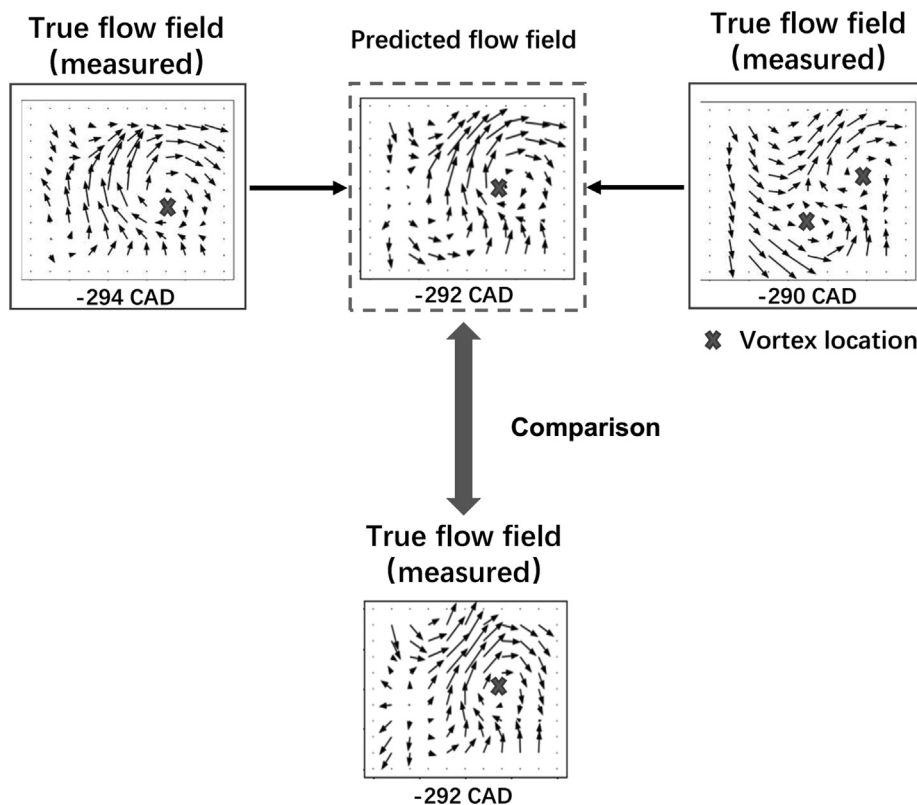


Fig. 5. An illustration of time-sequenced flow field prediction and validation.

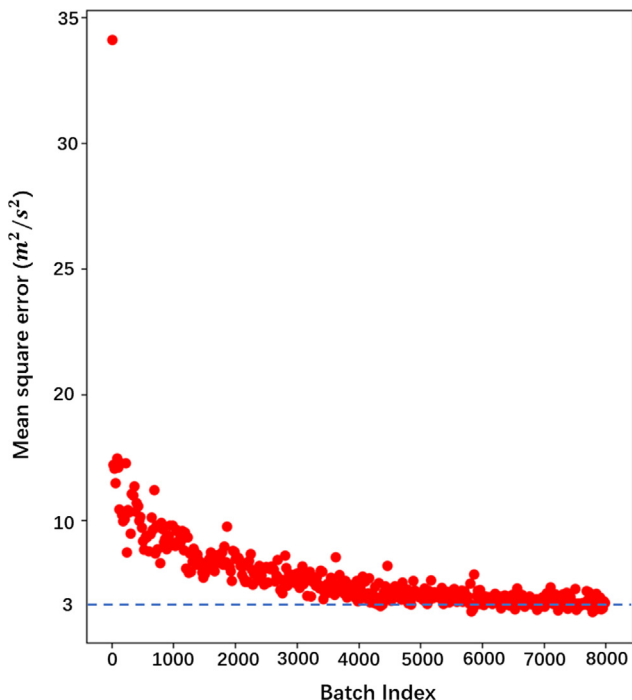


Fig. 6. Mean square error plot between true velocity vectors and predicted velocity vectors.

The data from the first and third crank angle constitute the input sequence. The data from the middle crank angle constitute the target flow field used to validate the output results.

For instance, the flow data at -294 CAD, -292 CAD and -290 CAD in Fig. 5 make up a group. The flow data at -294 and -290 CAD are the input sequence. The measured flow field at -292 CAD is used to

evaluate the prediction performance of the model. With every input in the training set, the weights are updated to minimize the MSE between the target flow field and output. Fig. 6 shows the MSE (loss function) plot between true velocity vectors and predicted velocity vectors using bi-RNN model during the training process. The batch size of the optimization is 100 and the training is stopped after 8000 iterations to prevent overfitting. The learning rate is set as  $3e-4$  as best practice. After the training process, the unseen test data are applied to validate the trained bi-RNN learner. With the prediction results from the test data, a bias-variance trade-off procedure is needed next to determine the reliability of this trained bi-RNN model.

### 3.3.2. Bias-variance trade-off

After the training process of the bi-RNN model, the training set and the 20% unseen data in the training process (test set) are both given to the model to generate prediction results. Afterwards, the global comparison indices between predicted and true flow fields of both training and test sets are calculated to show the bias-variation trade-off of this model. Achieving low bias and low variance is the goal of any supervised machine learning algorithms. However, there is always a trade-off between a model's abilities to minimize bias and variance. Bias means the difference between the averaged prediction value and the true value. High bias would cause under-fitting, which leads to high error between the training and test sets. This level of error occurs because the high-bias model does not pay a lot of attention to the training data and makes simplifying assumptions to make the target function easier to learn. In this study, our model can be considered to have low bias if both the GSI and GMI of the training set and test set are high and comparable. Variance shows the variability of model prediction for a given dataset. High variance would cause over-fitting. As a result, the high-variance model performs well on training data but has high error rates on test data. The reason is that the model with high variance pays too much attention to the training data, so that it cannot predict well using the data that it has not seen before. The standard deviations for

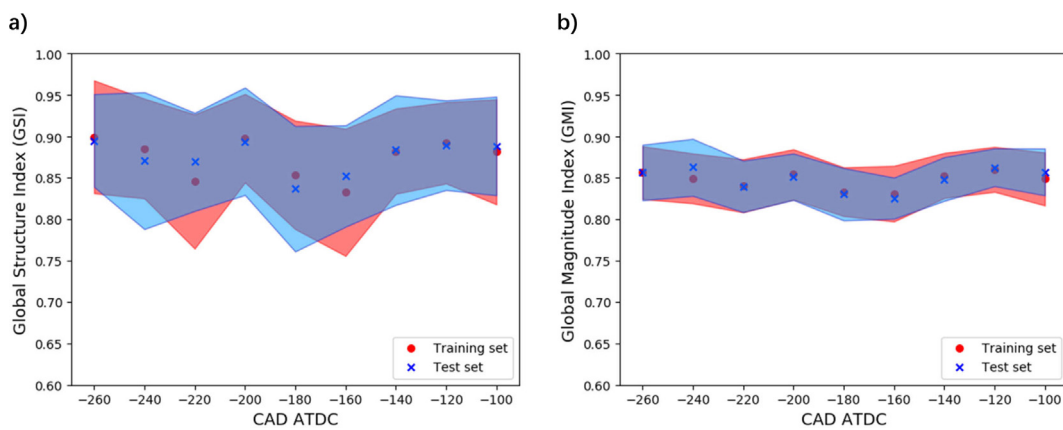


**Fig. 7.** Bias and variance check (mean  $\pm$  standard deviation) based on (a) GSI and (b) GMI values.

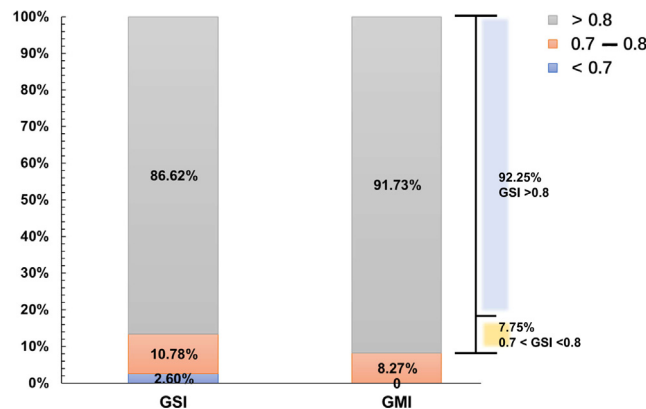
both the GSI and GMI are calculated to check the variance of our model.

Fig. 7 shows global comparison results (mean  $\pm$  standard deviation) of training and test sets at nine representative crank angles, i.e.,  $-260$  CAD,  $-240$  CAD,  $-220$  CAD,  $-200$  CAD,  $-180$  CAD (bottom dead center (BDC)),  $-160$  CAD,  $-140$  CAD,  $-120$  CAD, and  $-100$  CAD. Fig. 7 shows that both global comparison indices exceed 0.8 and the differences between the training and test sets are within 5%, showing that the bi-RNN model has low bias. Additionally, the standard deviations (the color bands in Fig. 7) of the GSI and GMI show an acceptable variance error for our model. From the results, both GSI and GMI comparisons exhibit a good bias-variance trade-off from intake stroke to compression stroke. In the following section, this trained model is employed to generate the target flow fields for detailed comparison and analysis.

#### 4. Results and discussion

##### 4.1. Global comparison

With this well-trained prediction model, a detailed comparison is conducted both globally and locally. The histogram in Fig. 8 shows the GSI and GMI value distributions of all the datasets. The data points are divided into 3 groups, whose GSI/GMI values are greater than 0.8, between 0.7 and 0.8, or smaller than 0.7. According to the global comparison histogram, the data points with the GSI and GMI values greater than 0.8 represent large proportions of 86.62% and 91.73%, respectively. The prediction accuracy of flow structure is relatively lower than the magnitude prediction since the output of the model is a vector  $\bar{v}_{(x,y)} = (v_x, v_y)$ , which is the velocity magnitude in x and y directions. The velocity direction is not directly predicted by the model but further calculated by the velocity magnitude  $v_x$  and  $v_y$ . In general,



**Fig. 8.** GSI and GMI values distribution.

this observation reveals that the majority of the predicted flow fields are in good agreement with the true flow data. Comparing with our previous study using large-eddy simulation (LES) to model the same SIDI engine, the flow field agreements using bi-RNN in the current study are better whereas the average GSI and GMI values of LES prediction are only 0.535 and 0.850, respectively [39]. However, there are still a few data points having relatively lower global comparison index values. For the GSI results, 2.60% of the data have values lower than 0.7. To further investigate the relations between GSI and GMI values, Fig. 8 also shows the GSI value distribution among the data points whose GMI values are greater than 0.8. The majority (92.25%) of the data points with  $GMI > 0.8$  also have  $GSI > 0.8$ . All the  $GSI < 0.7$  result in  $GMI < 0.8$ . The results show that the similarities regarding flow structure and magnitude are positively related. Poor agreement of flow structures between predicted and true flow fields will cause low similarities in flow magnitudes as well.

Next, a box plot is applied for more detailed analysis of the GSI/GMI dispersion and variations at different crank angles as well as determination of the outliers for those data points with low GSI/GMI values. As shown in Fig. 9a, a box plot uses five parameters to summarize a dataset: median, 25th percentile (Q1), 75th percentile (Q3), and minimum and maximum values; the difference value between Q3 and Q1 is the interquartile range (IQR). The data points located outside the range from  $Q1 - 1.5 \times IQR$  to  $Q3 + 1.5 \times IQR$  are treated as outliers. Fig. 9b and c are the global structure and magnitude comparison box plots in terms of the total dataset of 100 cycles. The same CADs shown in Fig. 7 from the intake stroke to the compression stroke are selected. Table 2 summarizes the information on the outliers at nine CADs from the intake to the compression stroke.

During early intake and late compression strokes, the global comparisons show great agreement between true and predicted flow fields. The median values of GSI and GMI are larger than 0.85. However, the GSI and GMI at BDC and later  $-160$  CAD are relatively lower, and the outliers are mostly located near  $-180$  CAD. The low similarity of prediction at  $-180$  and  $-160$  CAD could be caused by the reversed motion of the piston, resulting in more fluctuations of the in-cylinder flow. The reverse motion of piston starts at  $-180$  CAD, so the reductions in global index are clearly shown from  $-180$  CAD to  $-160$  CAD in both the GSI and GMI boxplots. During the early intake stroke, the intake valves are fully open and the strong inertia of intake air makes the in-cylinder flow prediction easier. For the late compression stroke, the intake valves are fully closed at around  $-140$  CAD and the upward piston movement is the main driver impacting the in-cylinder flow, which is also a simpler scenario than the cases around BDC.

In general, the majority of the indices of both structure and magnitude comparison are over 0.8 as depicted in the histogram in Fig. 8. The box plot results show that the structure and magnitude predictions

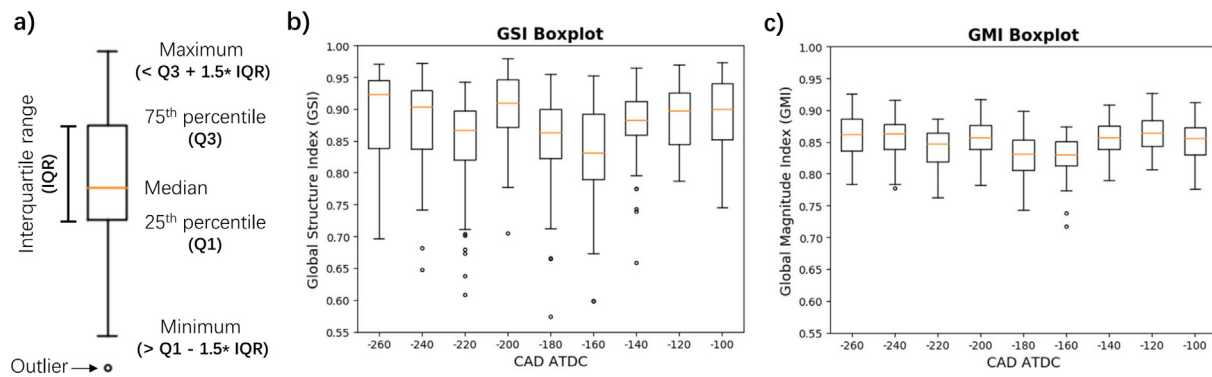


**Fig. 9.** (a) Box plot sample, (b) training set box plots, and (c) test set box plots.

**Table 2**

Summary of outliers in GSI and GMI boxplots.

CAD	-260	-240	-220	-200	-180	-160	-140	-120	-100
Num_GSI_Outliers	0	2	7	1	2	1	4	0	0
Mean_GSI_outliers	-	0.6646	0.6673	0.7042	0.6348	0.5984	0.7382	-	-
Num_GMI_Outliers	0	1	0	0	0	2	0	0	0
Mean_GMI_outliers	-	0.7774	-	-	-	0.7278	-	-	-

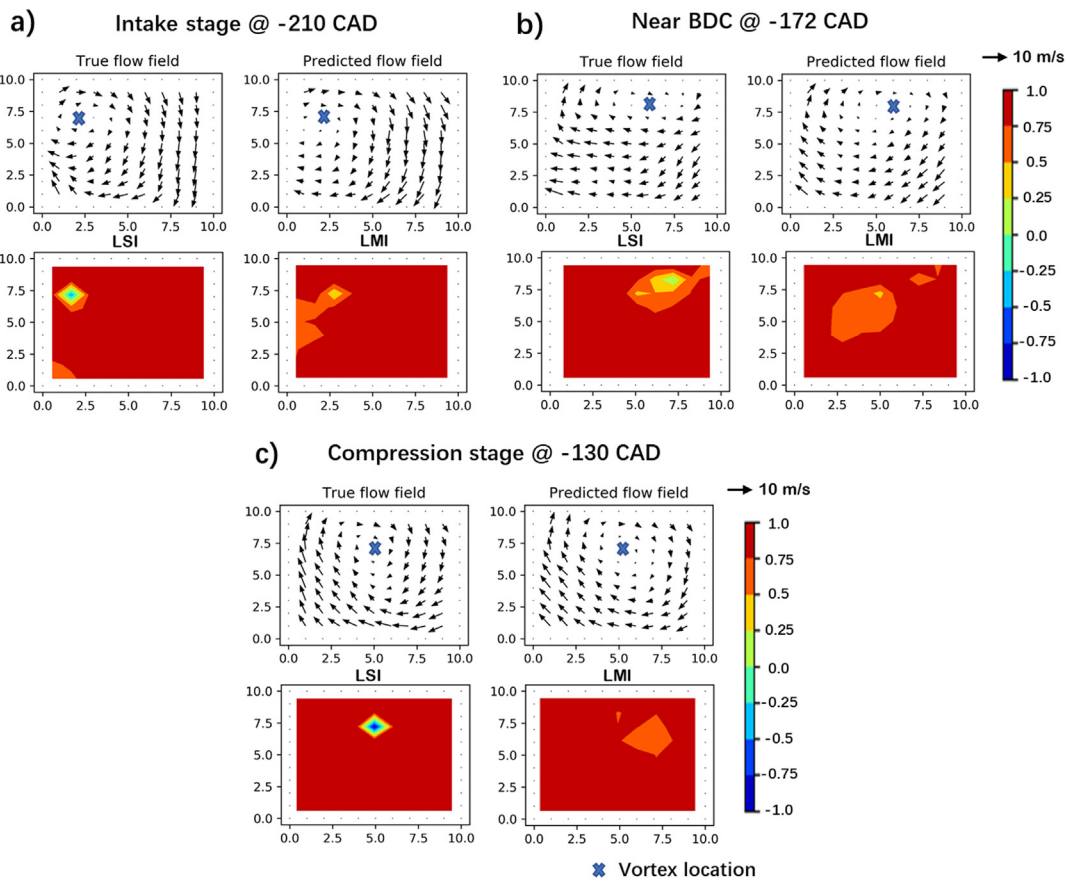


**Fig. 10.** LSI and LMI maps of the following cases: (a) GSI = 0.933 & GMI = 0.884; (b) GSI = 0.864 & GMI = 0.881; (c) GSI = 0.893 & GMI = 0.885.

at BDC are not as good as the predictions during the early intake stroke and compression stroke. In both the histogram and box plot results, better agreement is seen in the GMI comparison than in the GSI comparison. The percentage of outliers in the GMI comparison (0.33%) is much less than that in the GSI comparison (1.7%), and the range of the outliers is greater for GMI than GSI. However, GSI and GMI are only single numbers to quantify the flow similarities, which are not

informative enough to show the spatial details of the comparison. Thus, a point-by-point comparison is conducted next to show what the predicted and true flow fields may compare against each other with the presence of different GSI and GMI values.

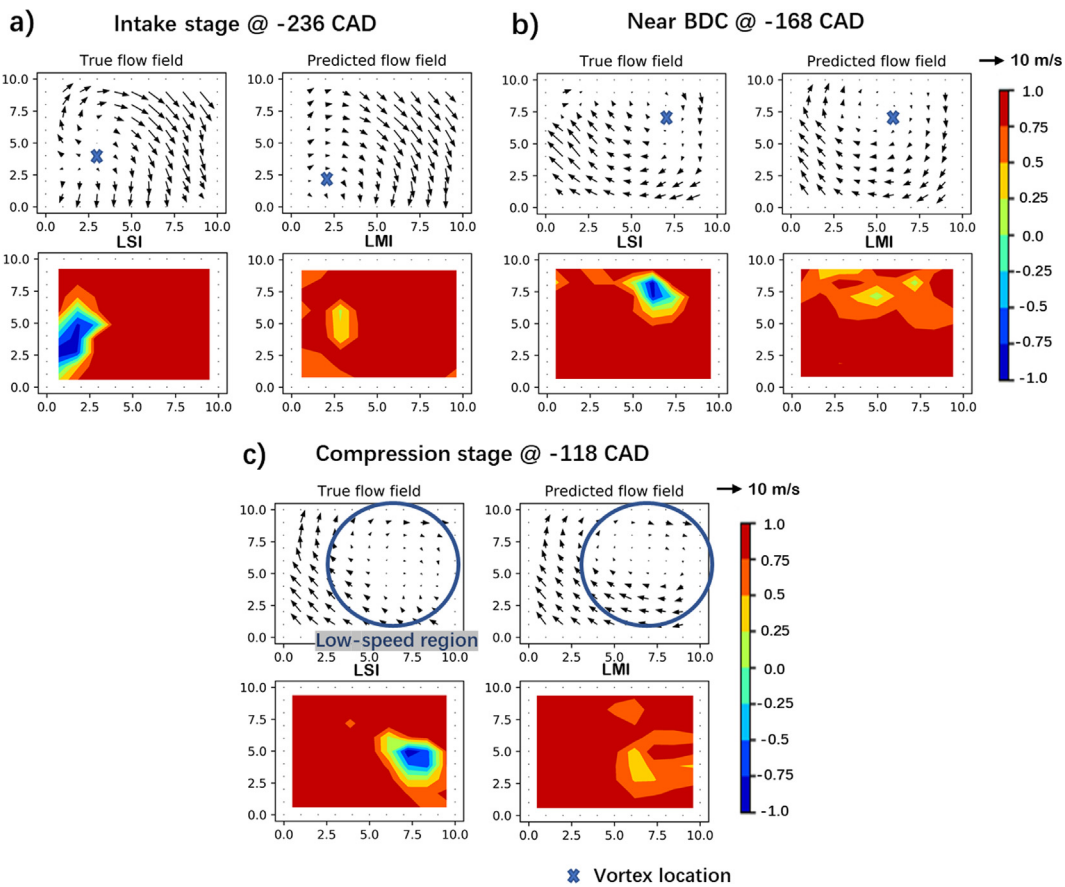


**Fig. 11.** LSI and LMI maps of the following cases: (a) GSI = 0.770 & GMI = 0.840; (b) GSI = 0.784 & GMI = 0.810; (c) GSI = 0.718 & GMI = 0.832. Circles highlight the low-speed regions.

#### 4.2. Local comparison

To clearly show details of flow comparison of different GSI/GMI values, local index contour maps are used to evaluate the similarity of each vector of the flow fields in this section. From the global comparison results, only 8.27% of GMI values are lower than 0.8, and most of the poor matching cases of flow magnitude are positively correlated with the poor prediction of the flow structures. Thus, this section will be divided into 3 parts by the GSI values: 1) GSI great than 0.8, 2) GSI between 0.7 and 0.8, and 3) GSI less than 0.7.

##### 4.2.1. GSI greater than 0.8

According to the global comparison results, the majority of the GSIs and GMIs are over 0.8. Therefore, the LSI and LMI maps of samples from intake stroke to compression stroke with global indices larger than 0.8 are shown in Fig. 10.

The local comparison results indicate that the model can predict well for bulk flow as well as vortex location. However, the vectors near the vortex center are seen to encounter high variations, since the velocity magnitudes are usually small at such locations. Velocity vectors with small magnitude are more easily affected by their surroundings, so the mismatches between the predicted and true flow fields are usually found at these locations. In general, the comparisons showing GSI and GMI larger than 0.8 indicate predictable cases which have a high accuracy. The predicted flow fields are acceptable in terms of both the flow structure and the magnitude comparison.

##### 4.2.2. GSI between 0.7 and 0.8

Except for the outliers, the minimum GSI and GMI are mainly located between 0.7 and 0.8. Fig. 11 shows the local comparison maps for

these datasets with relatively lower GSI and GMI. As in Fig. 10, the dissimilar regions are still located near the vortex center location. However, the dissimilar regions become larger compared with the cases in Fig. 10, so that the GSI decreases slightly. From the 2D plots, two reasons for the GSI reduction can be identified for most of the cases. First, the prediction of the vortex center locations is not very precise (see intake and BDC results in Fig. 11). Thus a small difference in vortex center locations could result in a large reduction in GSI. Second, large low-speed regions exist in flow fields (see compression results in Fig. 11). Although the locations of the low-speed regions are correctly predicted, the point-by-point velocity directions of small-magnitude vectors are harder to predict with high accuracy.

To further evaluate the influences of such low-similarity cases, the vorticity and kinetic energy (KE) are utilized to check the differences of flow feature. These key flow features could provide complementary information to the flow field comparison. Fig. 12 shows the average vorticity and KE curves of the data points with GSI ranging from 0.7 to 0.8 for each cycle. The X-axis indicates the cycle number. The correlation coefficient R represents the goodness of the data matching. A near perfect match has an R value approaching 1. From Fig. 12, the vorticity and KE are well-predicted for all cycles except for some peak points. These peak points are hard to be matched point-by-point for the cases with GSI ranging from 0.7 to 0.8 since the existence of dissimilar regions around vortex center locations and small-magnitude velocities highly affect the vorticity and KE values. However, the R values of vorticity and KE curves are high, which are 0.838 and 0.916, respectively. This finding indicates that the bi-RNN model is able to sufficiently capture flow features like vorticity and KE even though the velocity vectors of the prediction are not perfectly matched. In addition, it is proven that the bi-RNN model can also capture the cyclic variation

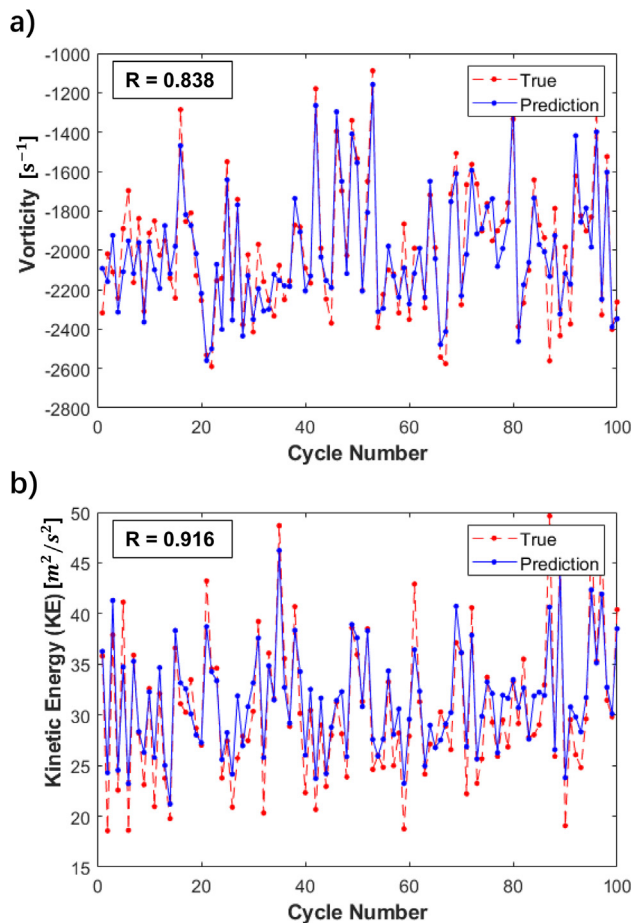


Fig. 12. (a) Vorticity and (b) KE curves for the cases of GSI between 0.7 and 0.8.

characteristics of the flow fields according to precise prediction of the vorticity and KE fluctuations in Fig. 12.

Fig. 13 shows detailed vorticity and KE maps of the two typical cases with GSI between 0.7 and 0.8, which show a slight shift in the vortex center location and a large region of low magnitude vectors, respectively. Fig. 13a and b show the same cases as in Fig. 11, near BDC and at the compression stage. According to the results, these two cases do not present significant differences in the vorticity and KE maps between the predicted and true flow fields. Thus, for the cases with slightly lower GSI values between 0.7 and 0.8, the velocity vector

differences usually do not affect flow feature analysis. These prediction results are still acceptable for in-cylinder flow transient dynamic analysis.

#### 4.2.3. GSI less than 0.7

For the cases with GSI below 0.7, most are treated as outliers by the box-plot criteria and are located near BDC. The GMI values of these outliers are also lower than the majority of the data points, which cannot reach 0.8. Fig. 14 shows the LSI and LMI maps of two cases with GSI less than 0.7 near BDC. The results show that the poor matching is caused by the inaccurate predictions of the vortex area and the low-speed region.

Next, the vorticity and KE curves are also utilized to check the flow-feature relevance of the cases with GSI below 0.7. Instead of showing the average vorticity and KE values of each cycle as in Fig. 12, the vorticity and KE values of every case with GSI less than 0.7 are shown in Fig. 15, since some cycles do not have any such low GSI cases. The results show that the model is still able to capture the overall trend in the vorticity and KE curves. However, considerable deviations are seen in the comparison of true and predicted vorticity magnitudes, while the agreement in the KE curves is still found to be good. Accordingly, the R values are 0.736 for the vorticity curves and 0.926 for the KE curves. The deterioration of model performance in predicting vorticity is attributed to the fact that the flow structures of these poorly matched cases are more complex than the ones shown in Fig. 12. The cases in Fig. 12 mostly correspond to strong single-direction vortex motions in the bulk flow, as indicated by the large absolute value of averaged vorticities. On the other hand, the absolute vorticity values in Fig. 15 are relatively close to zero. The finding of vorticity values approaching zero indicates that either the bulk flow breaks down into several small pockets with both clockwise and counterclockwise motions, or the vortex motion is extremely weak. Therefore, the flow field of these poorly matched cases is not simply dominated by a large-scale vortex motion, as in the cases with GSI larger than 0.7, and presents more spatial variations, thus posing difficulties in model prediction.

For detailed comparisons of flow features with spatial information, Fig. 16 shows vorticity and KE maps of an example whose GSI is below 0.7. With incorrect vortex and low-speed area predictions, the vorticity and KE inside the circled regions show poor agreement. This kind of predicted result gives wrong information about in-cylinder flow characteristics. As shown in Fig. 16b, the vorticity map of the true flow field shows a counterclockwise-dominant structure inside the circled region (vorticity > 0), while the whole predicted flow field shows a clockwise-dominant structure (vorticity < 0). The circled areas of the KE maps also show clear differences between the magnitudes of the velocity vectors. In general, the cases with GSI below 0.7 provide incorrect

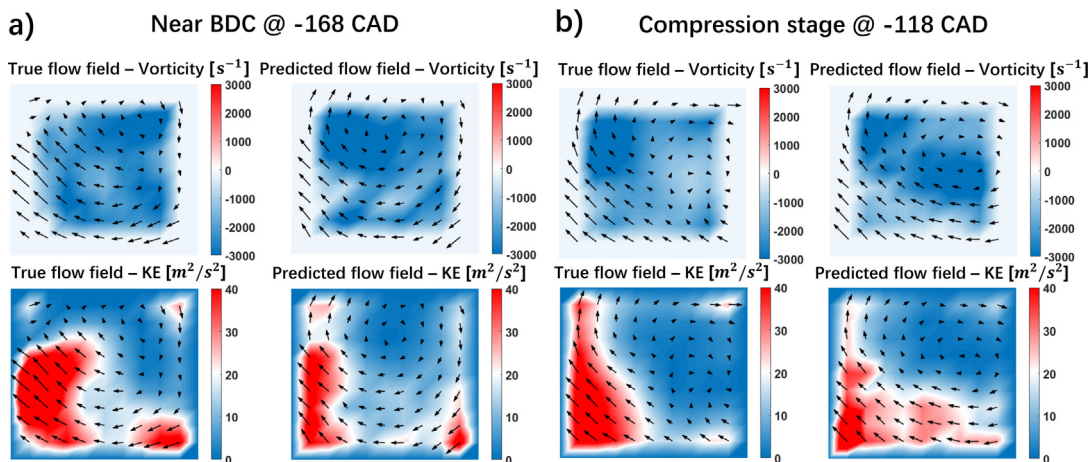


Fig. 13. Vorticity and KE maps of the cases with (a) a slight shift in vortex center location and (b) a large region of low-speed vectors.

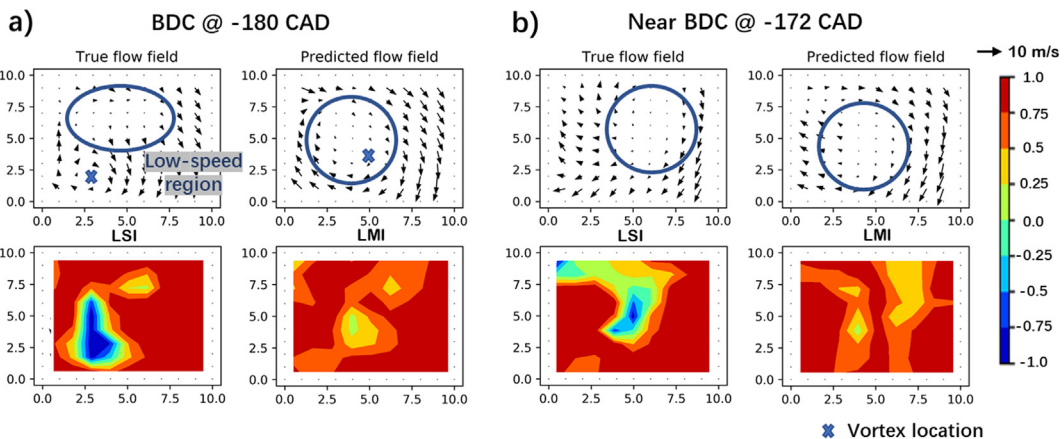


Fig. 14. LSI and LMI maps of the cases with (a)  $GSI = 0.565$  and  $GMI = 0.768$ ; (b)  $GSI = 0.663$  and  $GMI = 0.744$ . Circles highlight the low-speed regions.

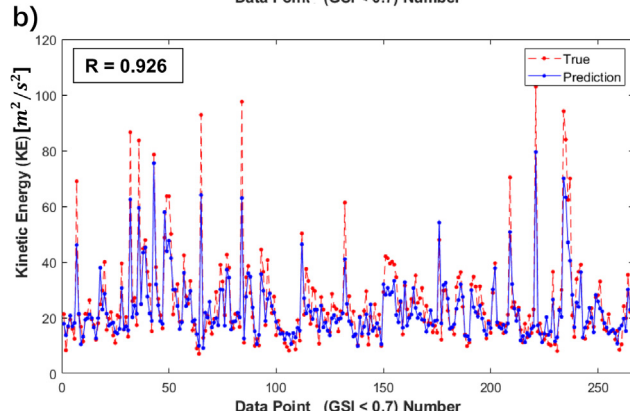
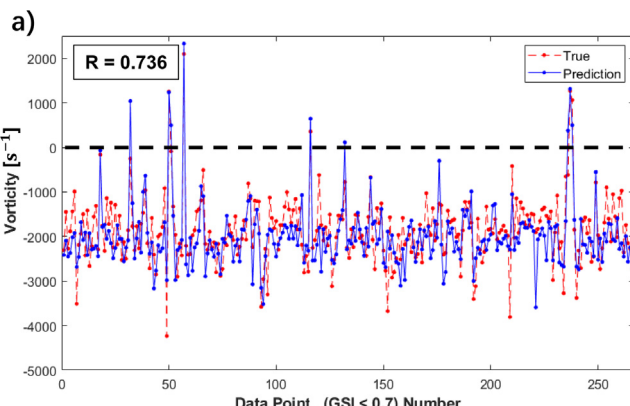


Fig. 15. (a) Vorticity and (b) KE curves for the cases of  $GSI < 0.7$ .

information on the locations of vortex motion and low-speed regions, and are considered unacceptable for flow-field prediction and flow-feature analysis. To overcome the poor vortex and low-speed region prediction around BDC, providing more flow data for training or extending the input sequence near BDC could help to improve the performance of the model.

In conclusion, the bi-RNN model can predict the bulk flow of all the cases from the early intake stroke ( $-298$  CAD) to the compression stroke ( $-100$  CAD). The global comparison results show that the prediction results at the early intake stroke and the compression stroke are better than for the cases around BDC. More outliers exist at the CADs near BDC, but the percentages of the outliers are reasonable for both GSI and GMI comparisons (1.7% for GSI and 0.3% for GMI). In general, the overall accuracy ( $GSI$  and  $GMI > 0.7$  except for some outliers) for all data points is acceptable, which is proven to be good enough for

transient flow feature analysis from global and local comparison results. In addition, local comparison results reveal that the inaccurate predictions about the vortex and low-speed area are the main sources of the low similarity between predicted and true flow fields.

## 5. Summary

In this study, a LSTM-based bi-RNN model was developed to predict the flow fields inside an engine cylinder at different time steps using 100 consecutive cycles of PIV data. Crank-angle-resolved velocity flow fields from  $-298$  CAD to  $-100$  CAD were investigated. The inputs of the bi-RNN model are flow fields with a crank angle difference of 4 CAD, and the flow field that has a 2-CAD lag relative to the first-time-step flow field is the output. To evaluate the similarity between true and predicted velocity fields, global and local comparison indices were used to quantify the flow-field agreements with respect to both vector direction and magnitude. According to the global comparison results, the majority of the GSI (86.62%) and GMI (91.73%) values are over 0.8. Even higher global indices of 0.9 can be reached, especially during the early intake stroke and compression stroke, which are of the most interest in studies of in-cylinder flow. With a detailed analysis of flow features and local comparisons, the overall accuracy of predictions with GSI higher than 0.7 was proven to be good enough for transient flow feature analysis. In general, the bi-RNN model presented in this work performs well in precise prediction of the bulk flow movement and vortex motions. As described previously, the large scale coherent flow structure, which contains the most of the fluctuating energy, is an important factor causing cyclic variations. This study demonstrates that the deep-learning model bi-RNN, which is widely used in NLP, has the potential to learn the underlying dynamics of flow interactions and regress the coherent flow evolution. A well-trained time-sequenced flow-field prediction model has the ability to predict the flow-field movement and help overcome the limits on PIV experiments by, e.g., improving the temporal resolution of the measurements without decreasing the spatial resolution and recorded cycles and eliminating the time lag between different measurement planes of quasi-simultaneous time-resolved multi-plane PIV [16].

For poorly matched cases with GSI lower than 0.7 (2.6%), it turns out that the low similarity is attributable to the incorrect prediction of the vortex center and locations of low-speed regions. To further improve the accuracy of the prediction model, a potential solution could be to enlarge the dataset size and to extend the input sequence, since the dataset used in this work is relatively small and shallow in terms of size and depth compared with normal machine learning tasks like NLP. Future work will attempt to build a more general prediction model using larger in-cylinder flow dataset at multiple operating conditions. In addition, the prediction model in this study is focused on an engine

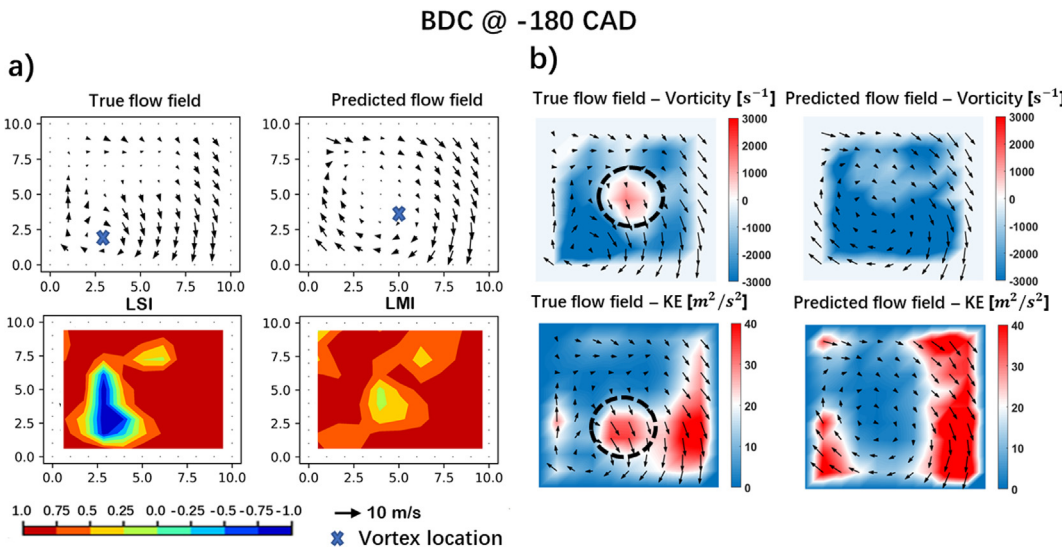


Fig. 16. (a) Plots of LSI and LMI, (b) vorticity and KE maps of an outlier at  $-180$  CAD ( $GSI = 0.565$  and  $GMI = 0.739$ ).

running under cold-flow (motoring) condition. For more complicated flow fields inside firing engines, the prediction could be more challenging due to larger temperature and composition variability. Therefore, more engine operation parameters such as engine speed, intake pressure, etc., can be added as inputs to achieve a deeper machine learning model that is applicable to more complex and practical engine running conditions.

#### Declaration of Competing Interest

The authors declare that they have no known competing financial interests or personal relationships that could have appeared to influence the work reported in this paper.

#### Acknowledgements

This research was carried out at the National Engineering Laboratory for Automotive Electronic Control Technology of Shanghai Jiao Tong University. The academic scholarship (201806230182) provided by the China Scholarship Council to Fengnian Zhao for his doctoral exchange study at Argonne National Laboratory is also acknowledged.

UChicago Argonne, LLC, operator of Argonne National Laboratory ("Argonne"), a U.S. Department of Energy Office of Science laboratory, is operated under Contract No. DE- AC02-06CH11357. The U.S. Government retains for itself, and others acting on its behalf, a paid-up nonexclusive, irrevocable worldwide license in said article to reproduce, prepare derivative works, distribute copies to the public, and perform publicly and display publicly, by or on behalf of the Government. This research was partially funded by DOE's Office of Vehicle Technologies, Office of Energy Efficiency and Renewable Energy under Contract No. DE-AC02- 06CH11357. The authors wish to thank Gurpreet Singh, Kevin Stork, and Michael Weismiller, program managers at DOE, for their support.

#### Appendix A. Supplementary material

Supplementary data to this article can be found online at <https://doi.org/10.1016/j.applthermaleng.2020.115253>.

#### References

- [1] J.L. Lumley, Engines: An Introduction, Cambridge University Press, 1999.
- [2] M. Mittal, D.L.S. Hung, G. Zhu, H. Schock, High-speed flow and combustion visualization to study the effects of charge motion control on fuel spray development and combustion inside a direct-injection spark-ignition engine, *SAE Int. J. Engines* 4 (2011) 1469–1480.
- [3] E. Porpattam, A. Ramesh, B. Nagalingam, Effect of swirl on the performance and combustion of a biogas fueled spark ignition engine, *Energy Convers. Manage.* 76 (2013) 463–471.
- [4] B. Peterson, D.L. Reuss, V. Sick, On the ignition and flame development in a spray-guided direct-injection spark-ignition engine, *Combust. Flame* 161 (1) (2014) 240–255.
- [5] N. Ozdor, M. Dulger, E. Sher, Cyclic variability in spark ignition engines-a literature survey, *SAE Paper* 940987, 1994.
- [6] G. Berkooz, *Turbulence, Coherent Structures, and Low-Dimensional Models*, Cornell University, Ithaca, New York, 1991.
- [7] K. Lee, D.E. Foster, Cycle-by-cycle variations in combustion and mixture concentration in the vicinity of spark plug gap, *SAE paper* 950814, 1995.
- [8] H. Shen, P.C. Hinze, J.B. Heywood, A study of cycle cycle-to-cycle variations in SI engines using a modified quasi-dimensional model, *SAE paper* 961187, 1996.
- [9] P. Drault, P. Guibert, F. Alizon, Use of proper orthogonal decomposition for time interpolation from PIV data. Application to the cycle-to-cycle variation analysis of in-cylinder engine flows, *Exp. Fluids* 39 (2005) 1009–1023.
- [10] A. Sakowitz, M. Mihaescu, L. Fuchs, Flow decomposition methods applied to the flow in an IC engine manifold, *Appl. Therm. Eng.* 65 (2014) 57–65.
- [11] T. Wang, W. Li, M. Jia, D. Liu, W. Qin, X. Zhang, Large-eddy simulation of in-cylinder flow in a DISI engine with charge motion control valve: Proper orthogonal decomposition analysis and cyclic variation, *Appl. Therm. Eng.* 75 (2015) 561–574.
- [12] J. Yang, M. Xu, D.L.S. Hung, Q. Wu, X. Dong, Influence of swirl ratio on fuel distribution and cyclic variation under flash boiling conditions in a spark ignition direct injection gasoline engine, *Energy Convers. Manage.* 138 (2017) 565–576.
- [13] H. Wei, X. Chen, G. Wang, L. Zhou, S. An, G. Shu, Effect of swirl flow on spray and combustion characteristics with heavy fuel oil under two-stroke marine engine relevant conditions, *Appl. Therm. Eng.* 124 (2017) 302–314.
- [14] H. Chen, M. Xu, D.L.S. Hung, H. Zhuang, Cycle-to-cycle variation analysis of early flame propagation in engine cylinder using proper orthogonal decomposition, *Exp. Therm. Fluid Sci.* 58 (2014) 48–55.
- [15] K. Lee, C. Bae, K. Kang, The effects of tumble and swirl flows on flame propagation in a four-valve S.I. engine, *Appl. Therm. Eng.* 27 (2007) 2122–2130.
- [16] J. Bode, J. Schorr, C. Krüger, A. Dreizler, B. Böhm, Influence of three-dimensional in-cylinder flows on cycle-to-cycle variations in a fired stratified DISI engine measured by time-resolved dual-plane PIV, *Proc. Combust. Inst.* 36 (3) (2016) 3477–3485.
- [17] Y. Li, H. Zhao, Z. Peng, N. Ladommato, Analysis of tumble and swirl motions in a four-valve SI engine, *SAE Technical Paper* 2001-01-3555, 2001.
- [18] F. Zhao, P. Ge, H. Zhuang, D.L.S. Hung, Analysis of crank angle-resolved vortex characteristics under high swirl condition in a spark-ignition direct-injection engine, *J. Eng. Gas Turbines Power* 140 (9) (2018) 092807.
- [19] E. Baum, B. Peterson, C. Surmann, D. Michaelis, B. Böhm, A. Dreizler, Investigation of the 3D flow field in an IC engine using tomographic PIV, *Proc. Combust. Inst.* 34 (2) (2013) 2903–2910.
- [20] F. Zhao, M. Liu, P. Ge, D.L.S. Hung, X. Li, M. Xu, X. Yang, C. Idicheria, Multi-plane time-resolved particle image velocimetry (PIV) flow field measurements in an optical spark-ignition direct-injection (SIDI) engine for large-eddy simulation (LES) model validations, *Oil Gas Sci. Technol.* 74 (2019) 52.
- [21] S. Buhl, F. Gleiss, M. Köhler, F. Hartmann, D. Messig, C. Brücker, C. Hasse, A combined numerical and experimental study of the 3D tumble structure and piston boundary layer development during the intake stroke of a gasoline engine, *Flow Turbul. Combust.* 98 (2) (2017) 579–600.

- [22] J. Kodavasal, A. Moiz, M. Ameen, S. Som, Using machine learning to analyze factors determining cycle-to-cycle variation in a spark-ignited gasoline engine, *J. Energy Resour. Technol.* 140 (10) (2018) 102204.
- [23] A. Hanuschkin, S. Schöberl, J. Bode, J. Schorr, B. Böhm, C. Krüger, S. Peters, Machine learning-based analysis of in-cylinder flow fields to predict combustion engine performance, *Int. J. Engine Res.* (2019), <https://doi.org/10.1177/1468087419833269>.
- [24] A. Moiz, P. Pal, S. Som, J. Kodavasal, D. Probst, Y. Pei, Y. Zhang, A machine learning-genetic algorithm (ML-GA) approach for rapid optimization using high performance computing, *SAE Int. J. Commer. Veh.* 11 (5) (2018) 291–306.
- [25] W. Yu, F. Zhao, W. Yang, H. Xu, Integrated analysis of CFD simulation data with K-means clustering algorithm for soot formation under varied combustion conditions, *Appl. Therm. Eng.* 153 (2019) 299–305.
- [26] Y. Pu, J. Reddy, S. Samuel, Machine learning for nano-scale particulate matter distribution from gasoline direct injection engine, *Appl. Therm. Eng.* 125 (2017) 336–345.
- [27] C. Sayin, H.M. Ertunc, M. Hosoz, I. Kilicaslan, M. Canakci, Performance and exhaust emissions of a gasoline engine using artificial neural network, *Appl. Therm. Eng.* 27 (2007) 46–54.
- [28] H. Taghavifar, H. Taghavifar, A. Mardani, A. Mohebbi, Modeling the impact of in-cylinder combustion parameters of DI engines on soot and NOx emissions at rated EGR levels using ANN approach, *Energy Convers. Manage.* 87 (2014) 1–9.
- [29] Y. Cay, Prediction of a gasoline engine performance with artificial neural network, *Fuel* 111 (2013) 324–331.
- [30] S. Roy, R. Banerjee, P. Bose, Performance and exhaust emissions prediction of a CRDI assisted single cylinder diesel engine coupled with EGR using artificial neural network, *Appl. Energy* 119 (2014) 330–340.
- [31] M. Kapusuz, H. Ozcan, J. Yamin, Research of performance on a spark ignition engine fueled by alcohol–gasoline blends using artificial neural networks, *Appl. Therm. Eng.* 91 (2015) 525–534.
- [32] M. Deb, P. Majumder, A. Majumder, S. Roy, R. Banerjee, Application of artificial intelligence (AI) in characterization of the performance-emission profile of a single cylinder CI engine operating with hydrogen in dual fuel mode: An ANN approach with fuzzy-logic based topology optimization, *Int. J. Hydrogen Energy* 41 (2016) 14330–14350.
- [33] G. Najafi, B. Ghobadian, A. Moosavian, T. Yusaf, R. Mamat, M. Kettner, W.H. Azmi, SVM and ANFIS for prediction of performance and exhaust emissions of a SI engine with gasoline–ethanol blended fuels, *Appl. Therm. Eng.* 95 (2016) 186–203.
- [34] S. Bhownik, R. Panua, S. Ghosh, D. Debroy, A. Pual, A comparative study of artificial intelligence based models to predict performance and emission characteristics of a single cylinder diesel engine fueled with Diesosenol, *J. Therm. Sci. Eng. Appl.* 10 (4) (2017) 041004.
- [35] S. Hochreiter, J. Schmidhuber, Long short-term memory, *Neural Comput.* 9 (1997) 1735.
- [36] H. Sak, A. Senior, F. Beaufays, Long short-term memory recurrent neural network architectures for large scale acoustic modeling, Fifteenth Annual Conference of the International Speech Communication Association, 2014.
- [37] X. Li, X. Wu, Constructing long short-term memory based deep recurrent neural networks for large vocabulary speech recognition, in: 2015 IEEE International Conference on Acoustics, Speech and Signal Processing (ICASSP). IEEE, 2005.
- [38] D.P. Kingma, J. Ba, Adam: A method for stochastic optimization, International Conference on Learning Representations 2015 arXiv: 1412.6980.
- [39] M. Liu, F. Zhao, X. Li, M. Xu, Z. Yue, S. Som, D. L.S. Hung, Systematic Multi-Index Validations of SIDI Engine Flow Field LES Computations Using Crank Angle-Resolved PIV Measurements, in: Proceedings of the ASME 2019 Internal Combustion Engine Division Fall Technical Conference. ICEF2019-7145, 2019.